



# EUROfusion

EUROFUSION WPHCD-PR(16) 16386

P. Veltri et al.

## **Ion beam transport: modeling and experimental measurements on a large negative ion source in view of the ITER heating neutral beam**

Preprint of Paper to be submitted for publication in  
Nuclear Fusion



This work has been carried out within the framework of the EUROfusion Consortium and has received funding from the Euratom research and training programme 2014-2018 under grant agreement No 633053. The views and opinions expressed herein do not necessarily reflect those of the European Commission.

This document is intended for publication in the open literature. It is made available on the clear understanding that it may not be further circulated and extracts or references may not be published prior to publication of the original when applicable, or without the consent of the Publications Officer, EUROfusion Programme Management Unit, Culham Science Centre, Abingdon, Oxon, OX14 3DB, UK or e-mail [Publications.Officer@euro-fusion.org](mailto:Publications.Officer@euro-fusion.org)

Enquiries about Copyright and reproduction should be addressed to the Publications Officer, EUROfusion Programme Management Unit, Culham Science Centre, Abingdon, Oxon, OX14 3DB, UK or e-mail [Publications.Officer@euro-fusion.org](mailto:Publications.Officer@euro-fusion.org)

The contents of this preprint and all other EUROfusion Preprints, Reports and Conference Papers are available to view online free at <http://www.euro-fusionscipub.org>. This site has full search facilities and e-mail alert options. In the JET specific papers the diagrams contained within the PDFs on this site are hyperlinked

# Ion beam transport: modeling and experimental measurements on a large negative ion source in view of the ITER heating neutral beam

P. Veltri<sup>1,2,a)</sup>, E. Sartori<sup>2,3</sup>, P. Agostinetti<sup>2</sup>, D. Aprile<sup>2</sup>, G. Chitarin<sup>2,3</sup>, N. Fonnesu<sup>4</sup>, K. Ikeda<sup>5</sup>, M. Kasaki<sup>5</sup>, H. Nakano<sup>5</sup>, A. Pimazzoni<sup>2</sup>, K. Tsumori<sup>5</sup> and G. Serianni<sup>2</sup>.

<sup>1</sup>*INFN-LNL, viale dell'Università n. 2, Legnaro, Italy*

<sup>2</sup>*Consorzio RFX (CNR, ENEA, INFN, Università di Padova, Acciaierie Venete SpA), C.so Stati Uniti 4, Padova, Italy.*

<sup>3</sup>*Dept. of Management and Engineering, Università. di Padova, Vicenza, Italy*

<sup>4</sup>*Department of Industrial Engineering, University of Rome "Tor Vergata", Via del Politecnico 1, Rome, Italy*

<sup>5</sup>*National Institute for Fusion Science, 322-6 Oroshi, Toki, Gifu 509-5292, Japan*

<sup>a)</sup>Corresponding author: pierluigi.veltri@igi.cnr.it

**Abstract.** Neutral beam injectors are among the most important methods of plasma heating in magnetic confinement fusion devices. The propagation of the negative ions, prior to their conversion into neutrals is of fundamental importance in determining the properties of the beam, such as its long-distance aiming and focusing, so as to deposit the beam power in the proper position inside the confined plasma as well as to avoid interaction with the material surfaces along the beam path. The final design of the ITER Heating Neutral Beam prototype has been completed at Consorzio RFX (Padova, Italy), in the framework of a close collaboration with European, Japanese and Indian fusion research institutes. The physical and technical rationales on which the design is based were essentially driven by numerical modelling of the relevant physical processes, and the same models and codes will be useful to design the DEMO neutral beam injector in the near future. This contribution presents a benchmark study of codes used to this purpose, by comparing their results against an existing large-power device, hosted at the National Institute for Fusion Science (NIFS), Japan. In particular, the negative ion formation and acceleration are investigated. A satisfactory agreement was found between codes and experiments, leading to an improved understanding of beam transport dynamics. The interpretation of the discrepancies identified in previous works, possibly related to the non-uniformity of the extracted negative ion current, is also presented.

## 1. INTRODUCTION

Modelling of negative ion sources necessarily entails a wide range of phenomena, from the Plasma-RF coupling [1], [2], [3], to the particle dynamics in the source [4], [5] from the cesium dynamics [6] to the negative ion extraction [7], [8], [9] [10]. The difficulty to directly diagnose in a separate manner the involved phenomena poses serious limitations to the comparison between codes and experiments; although in recent years models have been reaching a higher maturity, the physics of several processes is still debated.

Negative ion beam formation and transport, on the other hand, seems better understood and the development of dedicated numerical tools (based on ray tracing and Monte Carlo approaches) was often simply a modification of codes originally developed for positive ion or electron beams [11], [12] by including some specific features of negative ions, such as the electron detachment and the presence of electron space charge. These approximations sufficed to achieve stability of numerical trends and reproducibility of results. Moreover a benchmark of acceleration and transport codes with real experiments showed in general a satisfactory overall agreement with the

measurements performed in existing negative ion accelerators [13], [14], [15], motivating their massive employment in the design phase of the future neutral beam injector of fusion experiments like ITER and DEMO.

Nonetheless, significant discrepancies are routinely found between codes and experiments. The origin of such specific discrepancies, which might non-negligibly affect the performances of large beams propagating tens of meters before reaching the plasma, is still to be understood. A more comprehensive benchmark of the codes is required to assess their actual degree of reliability, interpreting measurements in future experimental devices. The aim of this paper is to verify the numerical results against data collected in a real negative ion accelerator whose design is quite close to the ITER NBI design. To this purpose, a diagnostic calorimeter designed at Consorzio RFX was installed in one of the most powerful existing negative ion sources, the R&D negative ion source (RNIS) of the NIFS (Toki, Japan) NBI team. In the paper, measurements and simulations are for hydrogen ions.

This paper is organized as follows: in section 2 the suite of numerical codes used for the beam transport modelling is described. Section 3 deals with the experimental equipment used to benchmark the codes; section 4 reports on the codes not directly related with the beam transport, but needed for a correct modelling of the beam itself; section 5, finally, deals with the beam transport along the accelerator and the beamline.

## 2. NUMERICAL TOOLS

Among the numerical tools used for designing the heating neutral beam injector of ITER [16], [17] and its full scale prototype MITICA [18], [19], an important role was played by the ray tracing codes describing the beam transport inside the accelerator and the beamline. In this sense, a fundamental tool was the OPERA 3D code [12], capable of a steady-state solution of the equation of motion of particles moving in self-consistent electromagnetic fields, taking into account their own space charge. This code implements a simplified model for the calculation of the plasma meniscus, i.e. the interface between the plasma (containing the negative hydrogen ions) and the beam; it imposes a vanishing electric field inside the plasma, connected to the region of high potential gradient inside the accelerator. The code takes as input the geometry and voltage of the electrodes and the extracted current density. An iterative approach between the stationary solution of the Poisson equation and the ray tracing of a finite number of test particles for the space charge distribution is adopted, and the scheme usually reaches the convergence in few iterations. The space charge of co-extracted electrons is not included in the simulations: this is because in well-conditioned caesiated sources, electrons represent less than 50% of the total extracted current; hence, due to their higher mobility (lower density), their space charge is negligible with respect to the space charge of negative ions. Beam averaged quantities, such as the beam emittance, angular deflection and divergence, are calculated from particle positions and velocities at a chosen location in the accelerator to be compared with indirect measurements of the same quantities.

Alternative numerical codes for beam acceleration, such as SLACCAD [11], BYPO [20], and ACCPIC [21], offer a more detailed model of beam formation and transport at the cost of assuming simplified 2D (axisymmetric or Cartesian) electric field distributions. However the intrinsic three-dimensionality of our benchmark case, due to the grid geometry and to the presence of a complex external magnetic field in the RNIS test stand, makes OPERA the most effective tool for the comparative studies of beam optics as reported in this paper (see section 3).

In many circumstances for which the axisymmetric approximation holds, the agreement of the axisymmetric codes with OPERA was reasonable. A more detailed study of these models and of the assumptions on which these codes are based, is outside the scope of this paper.

The motion of particles travelling inside the accelerator is influenced by the presence of permanent magnets embedded in the electrodes and in the ion source walls. The corresponding magnetic field  $B$  must be calculated and used as input during the ray tracing procedure just described. Even though the  $B$  field can be calculated by an additional package of OPERA, based on the finite element approach, we preferred to calculate the  $B$  field with the code NBIImag [22], developed at RFX. Its formulation is based on the efficient numerical integration of Biot-Savart law, and for this reason there is no need to map the air volume of the 3D domain, avoiding the numerical errors related to mesh size, typical of finite element codes. Other important features of NBIImag are that it does not produce errors related to the finite size of the domain, which due to its integral formulation is virtually infinite, and that it does not require complicated and time consuming matrix inversion, allowing a faster calculation of the results, even in case of complex magnetic field configurations produced by thousands of permanent magnets and current-carrying busbars.

The propagation of particles inside the accelerator is also subject to interactions with the background gas  $H_2$ , which is injected into the source to sustain the plasma, and flows through the accelerator apertures toward the beamline vessel, where pumping is usually installed. This interaction results in a loss of negative ion current, due to electron detachment from the  $H^-$ , and in the generation of stray particles with consequent heating of the electrodes. In this benchmark, we focused on the reduction of the beam current along the accelerator, which plays a role in the reduction of the beam space charge. This reduction must be considered when solving the Poisson equation, hence a profile of the background gas has to be estimated and the consequent current loss has to be introduced in OPERA. The gas profile was calculated with the AVOCADO code [23]. AVOCADO implements the well-known angular coefficient method [24], based on the decomposition of the geometrical domain in a set of surfaces, for which the mutual view factors are calculated. Then, pressure at walls and flows through boundary surfaces are calculated by solving a system of linear equations. The boundary surfaces where fixed pressures, gas flux or pumping speed are imposed, determine the values of the gas pressure in the rest of the domain. In AVOCADO, the gas density is then extrapolated at chosen points within the volume. The code was validated [25], benchmarked in small ion sources [26] and used in the ITER HNB design [17], [19] [27]. Using the externally calculated beam loss and magnetic field map, OPERA calculates an accurate distribution of the potential to compute the trajectories of negative ions.

The trajectories of secondary particles, that are useful to estimate the power load on the electrodes of the accelerator, can be more easily evaluated by other codes [28], [29], [30], without including their negligible space charge into the self-consistent calculation of the electric field. These codes use a Monte Carlo approach to describe the collisions of the beam with the residual gas and the solid surfaces of the accelerator, with appropriate models for the generation, emission and reflection of secondary particles. The beam motion is modelled according to prescribed electric and magnetic fields calculated a priori (by OPERA or similar tools). In particular, the EAMCC code [28] was employed to evaluate and minimize the heat loads on the accelerator grids of ITER HNB and therefore to optimize its magnet system and cooling circuit [17], [19], [31]. The original version of the code assumed an axial symmetric electric field and used a modular approach to decompose the accelerator domain: a single cell of the accelerator (one beamlet) was modelled with periodic boundary conditions on particle motion. In order to have a consistent description of the whole accelerator, the original version of EAMCC was modified to deal with more realistic 3D geometries and multi beamlet simulations [32], [33]. This upgraded version allows simulating the transport and interaction of all the 15 beamlets of a grid segment, from the meniscus to the impact with the diagnostic calorimeter.

### 3. EXPERIMENTAL SETUP

The experimental data used as benchmark for the numerical codes in the present paper were measured at the RNIS (Research and development Negative Ion Source) test stand, hosted at NIFS institute. The test stand is based on an arc-driven plasma source and accelerator, and is very similar by design to the ion beam sources used in Neutral Beam Injectors of the Large Helical Device experiment [34] [35]. The features of the RNIS source and acceleration system are listed below.:

- Production of negative ions ( $j_H$  in the  $300 \text{ A/m}^2$  range) from a plasma source having large surface area, by means of a gridded electrode (called plasma grid, PG) with tapered apertures, to enhance the negative ion yield by surface conversion;
- Extraction of negative ions through the PG by means of a second gridded electrode (called extraction grid, EG) polarized at a voltage of about +10 kV with respect to the PG ;
- Acceleration and focalization of negative ions through the second electrode towards the last electrode (named grounded grid, GG), with a maximum beam energy of 70 keV
- deflection of co-extracted electrons by means of permanent magnets embedded in the extraction grid;
- Propagation of the ion beam downstream of the last electrode inside a large chamber, (where the source gas is pumped) towards a gas-cell constituting the neutralizer.

Each grid is composed by two segments, featuring 238 apertures each, arranged in a 14x17 pattern. Moreover, the GG has slotted apertures, i.e. a single horizontal slot is shared between each row of beamlets, and the beam deflection (induced by the presence of magnets embedded in the EG) is recovered by electrostatic means, by applying the aperture displacement technique [34], [35], [36] to a dedicated electrode (Steering grid, SG) placed immediately downstream of the EG and polarized at the same potential. A different technique is in the ITER HNB

prototypes, where the deflection is recovered by using another set of magnets inserted in the GG [37], or additional magnets in the EG [38], [39].

The use of the slotted GG in RNIS induces a deviation in the beam optics: a 1D lens is formed so that the standard defocusing effect of the GG lens is ineffective in the horizontal x direction; this distortion results in the creation of elliptical beamlets, and it turns into the impossibility of simultaneously minimizing the beam divergence along both directions. To overcome this problem, the shape of the SG was modified, from the standard circular aperture into a sort of racetrack-shaped aperture [40], [41]; thanks to this modification, the focusing electrostatic lens that is formed on the SG is enhanced in the y direction and weakened in the x direction, compensating for the successive defocusing given by the slotted GG.

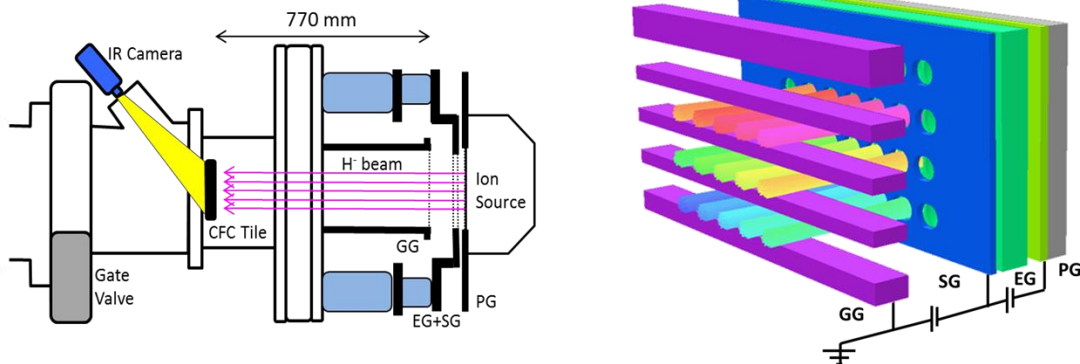


Figure 1 a) Schematic of the RNIS beamline, with the CFC calorimetric target mini-STRIKE (MS) installed, top view. b) Sketch of the accelerator domain (3x5 beamlets corresponding to the PG mask) used in the numerical simulations. The beamlet trajectories calculated by the OPERA code are also shown.

A calorimetric target was used as a diagnostic tool for measuring the properties of the accelerated negative ion beam. The target is a prototype of the STRIKE calorimeter, one of the diagnostics under construction for the SPIDER experiment [42] [43] [44]. This diagnostic target, named mini-STRIKE (MS) is placed at a distance of 0.77 m from the GG where it intercepts the beam. The active part of the target is constituted by a couple of unidirectional carbon-carbon fibre composite (CFC) tiles.

The carbon fibres of the CFC tiles are oriented so that the thermal conductivity along a direction perpendicular to the tile surface is more than 10 times larger than along the directions parallel to the surface. Thanks to this anisotropy, a direct correlation exists between the temperature distribution visible on the downstream surface of the tile and the power density profile deposited by the beamlets on the beam-facing upstream surface of the tile. As the size of each tile is 90x120 mm, only 15 beamlets per segment (arranged in a 3x5 matrix) were used, by applying a suitable mask to the PG entrance, in order to accommodate all of them within the limited tile surface. An infrared (IR) camera installed on a lateral viewport of the vessel was used to measure the temperature distribution on the downstream surface of the target tile. The infrared images of this thermal pattern are used to study the beamlet characteristics obtained in different source conditions as described in the following.

### 3.1. Analysis of infrared data

The IR camera acquisition covers the entire evolution of the beam pulse: before, during and after each beam extraction and acceleration; the beam-on duration is set to 1 second. Even though a transient analysis is possible (being only limited by the dynamic response of the CFC and the camera acquisition rate), for the purposes of this work the analysis of a single frame in comparison with a frame taken before the pulse was considered. This is because of the steady-state nature of the ray tracing code used for the benchmark. Usually the frame at which the temperature rise reaches its maximum is analysed, after removing the frame (or an average of some frames) before the beginning of the beam, which is treated as the background signal. The IR image is then corrected according to a homographic transform, to compensate for the perspective distortion caused by the view angle of the camera. The

data is then fitted with a 2D function  $f(x,y)$ . Many choices are possible for the fitting function; in this study we use a multi Gaussian function, i.e. the superposition of 15 Gaussians, each one having the standard 5 free parameters (amplitude  $A$ , horizontal and vertical centers  $x_0$  and  $y_0$  and width ( $\sigma_x$  and  $\sigma_y$ ).

The resulting fitting function is therefore expressed as:

$$f(x, y) = \sum_{i=1}^{15} A_i \exp \left[ - \left( \frac{(x - x_{0_i})^2}{\sqrt{2}\sigma_{x_i}} \right) - \left( \frac{(y - y_{0_i})^2}{\sqrt{2}\sigma_{y_i}} \right) \right] \quad (1).$$

An alternative and more complete analysis method, based on the transfer function method [44] has also been used. In this case the tile is considered as a dynamic system described by a transfer function which determines the relationship between the input (heat flux distribution  $F(x,y)$  on the upstream surface) to an output (temperature distribution  $T(x,y)$  on the downstream surface). Once the temperature distribution map  $T(x,y)$  is measured, it is possible to calculate its Fourier transform and multiply it by the inverse-transfer function. By calculating the inverse Fourier transform of this product (after proper filtering) the impinging flux  $F(x,y)$  can be determined. The inverse-transfer function is obtained as the tile response to a localized (spatial Dirac delta function) input. After reconstruction of  $F$  we can use a similar fitting function  $f$ , as expressed in equation (1) to fit the energy flux profile. The advantage of the transfer function method is that the reconstructed image of each beamlet footprint on the front is smaller than the measured one on the rear of the tile. Therefore, the fitting procedures are simplified. Figure 2 reports the raw IR data and the reconstructed energy flux profile, obtained with the transfer function method.

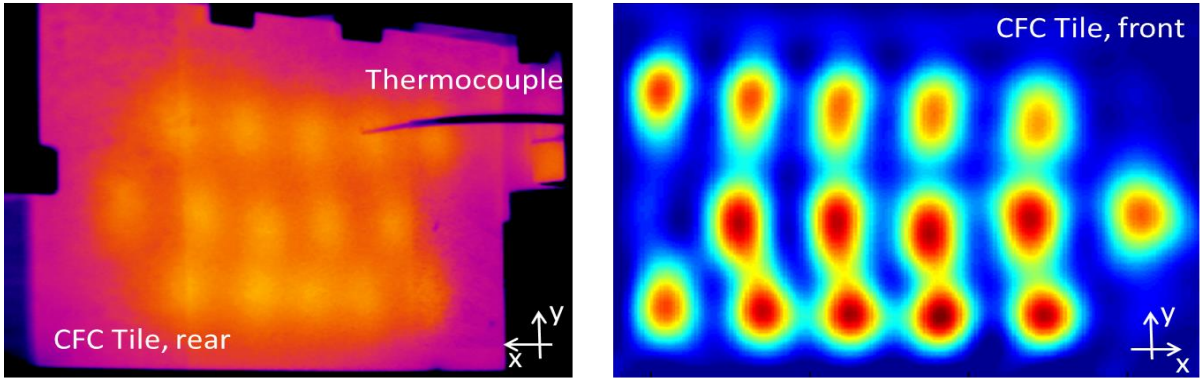


Figure 2 a) Raw IR image acquired by the thermal camera. Note the shading corresponding to a reference thermocouple in contact with the rear of the tile. b) The estimated power load on tile front, obtained by the IR data after post-processing (background removal, homographic transform and reconstruction by transfer function).

#### 4. NUMERICAL EVALUATION OF MAGNETIC FIELD AND GAS DENSITY DISTRIBUTION IN THE ACCELERATOR AND BEAM LINE VESSEL

Beam transport modelling requires some preliminary considerations on the parameters not directly measurable, as well as precise assumptions on the boundary conditions of the system. Among them, the magnetic field maps and the gas density distribution. In this section we present a validation of the codes that have been used for the evaluation of the magnetic field  $B$  and the gas density  $n_g$ .

## 4.1. Magnetic Fields

The codes simulating the magnetic fields are the easiest to validate, since they can be compared directly with the steady-state magnetic field measurement collected using a suitable probe [45] before initiating the beam operation. In the present test a Hall effect magnetic field probe (F.W Bell, model 5080) was used. The magnetic system of RNIS involves 30 bars of permanent magnets embedded in the EG, to deflect the co-extracted electrons, and 2 large magnets in the source lateral walls, to generate the transversal filter field necessary to lower the electron temperature in the vicinity of the extraction area. The magnets are sketched in Figure 3-a; the point  $z=0$  corresponds to the PG entrance position.

The measured values were compared with the B field simulated with the numerical codes OPERA and NBImag, described in section 2. The magnetic field profiles obtained by both codes are perfectly overlapped, with a small numerical noise noticeable in the low field components of the TOSCA simulation. When the measurements of the probe are compared with the numerical results of the codes, a satisfactory agreement is found: Figure 3b reports the values of measured and simulated data relative to the y component of the field, responsible for the deflection of electrons and ions. The two lines, labelled beam1 and beam2 identify the centre of two apertures along which the profiles were taken, belonging to two consecutive rows. The usual alternation of  $B_y$  peaks from row to row is evident.

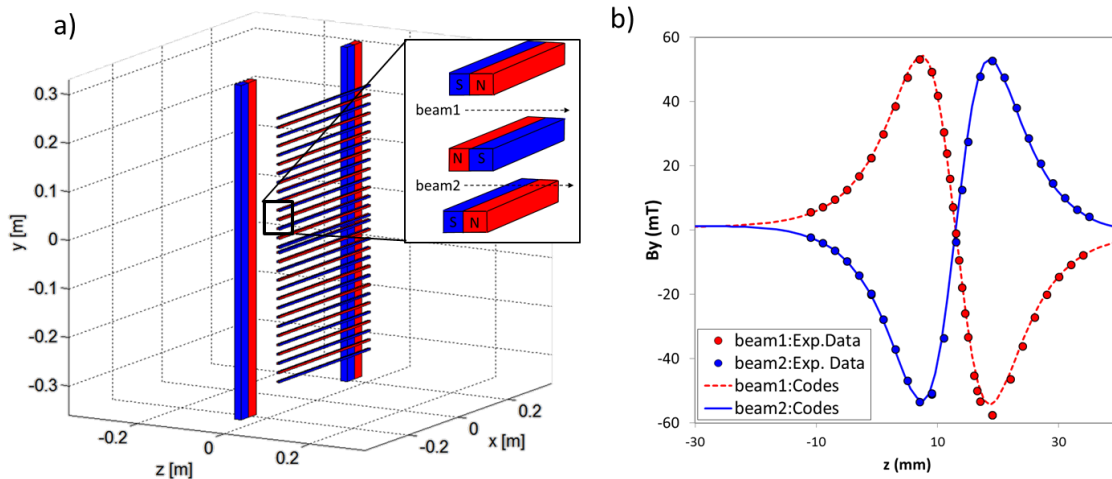


Figure 3 a) layout of the permanent magnets in the RNIS test stand (cusp magnets, not affecting the beam, are omitted for figure readability). The larger bars represent the magnets used for electron cooling (filter field) in the source, whereas the smaller horizontal magnets (closer view in the figure onset) are embedded in the EG and used to suppress the co-extracted electrons on the grid itself. In b) the magnetic field profile  $B_y$  calculated with the code NBIMAG (solid line) or measured with the Hall sensor are compared.

## 4.2. Neutral gas density distribution

The three-dimensional gas density distribution in a dynamic vacuum system is hard to measure directly. In the case of the NIFS test stand, the only available measurements consist in pressure gauges in the ion source and in the vessel, while the injected throughput is estimated indirectly from the metering valve settings. Given the limited amount of data available, and spread over the whole vacuum system, we decided to develop a numerical model of the whole ion source, accelerator, and vacuum vessel as shown in Figure 4(a). The model includes the geometrical details of the grid round apertures and slits, as shown in Figure 4(b). Hydrogen gas at room temperature is considered. Pressure in the ion source and in the vessel is imposed as boundary conditions, and the throughput results from the simulation; the vessel pressure is set three orders of magnitude lower than the ion source pressure. The normalized pressure distributions calculated with the AVOCADO code is shown in Figure 4(c,d), in which it is possible to notice the reduced PG conductance imposed by the 15 aperture mask.



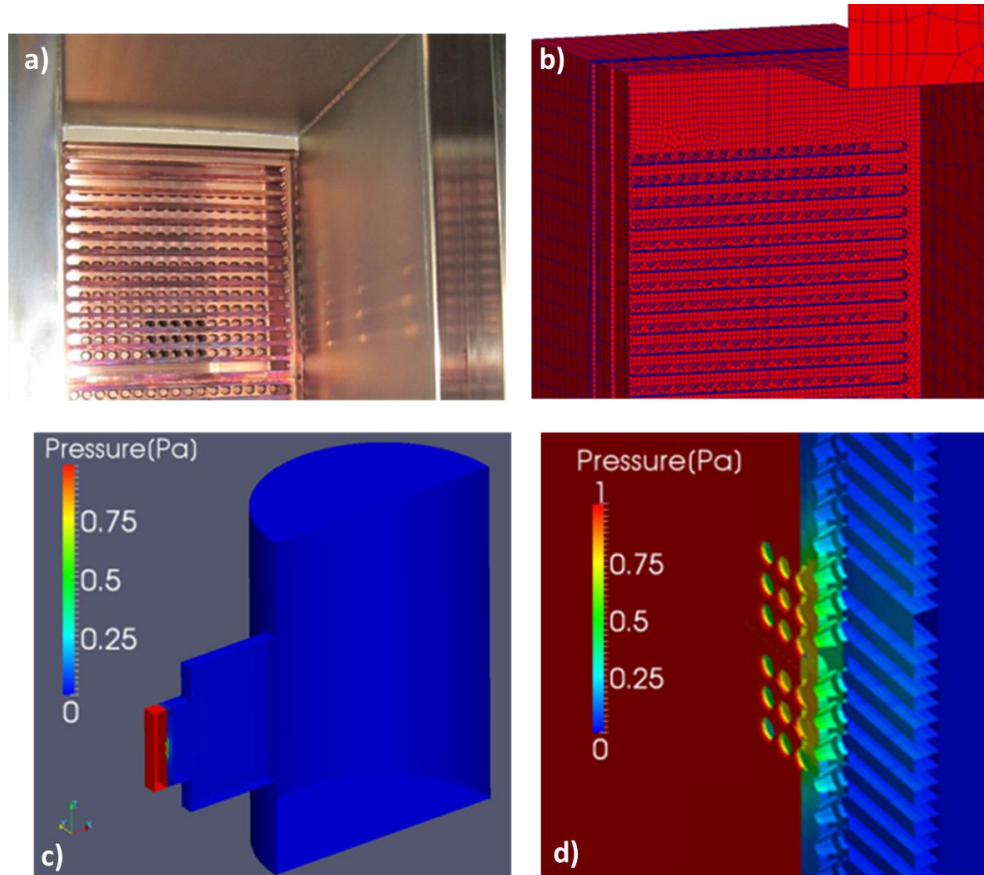


Figure 4 Gas density calculations: (a) view of the RNIS accelerator from the tank; (b) view of the accelerator in the full scale AVOCADO model of the ion source and vessel; (c) pressure distribution calculated with AVOCADO, section view of the whole model; (d) detail view of the pressure distribution in the accelerator.

The numerical results, calculated for steady state, are compared in Table 1 with experimental measurements, obtained in transient conditions. Due to this difference the experimental pressure measured in the source and in the vessel ( $P1$  and  $P2$ ) is lower by about 20%; the pressure measurement in the ion source did not reach a steady state even after 15s after valve opening, and understanding the reasons for this requires further investigations. Furthermore the experimental gas throughput is estimated by assuming a linear behaviour of the metering valve, in a low-opening regime (5% in this case) for which linearity is not guaranteed.

Table 1 Comparison of experimental measurements and simulation results.

	Measurement (transient)	Simulation (steady state)
$P1$ [Pa]	0.22	0.289
$P2$ [Pa]	0.001	0.0003
$\underline{Q}$ [Pa m <sup>3</sup> /s]	0.42	0.42
$C_{source,vessel}$ [m <sup>3</sup> /s]	1.93	1.46

The  $H_2$  density profile through the accelerator, which is needed to estimate the beam stripping losses, is shown in Figure 5 for a filling pressure of 0.3Pa. The calculation of stripping losses starts at the meniscus position ( $z=5$  mm in

the picture). The dominant process causing stripping loss is considered, that is single electron detachment by collision with molecular hydrogen  $\underline{H} + H_2 \rightarrow \underline{H} + H_2 + e$ . The cross section is obtained from [46] as a function of the particle energy. A total stripping loss of 12% at the exit of the accelerator is obtained, as shown in Figure 5 in the case of nominal extraction and acceleration voltages.

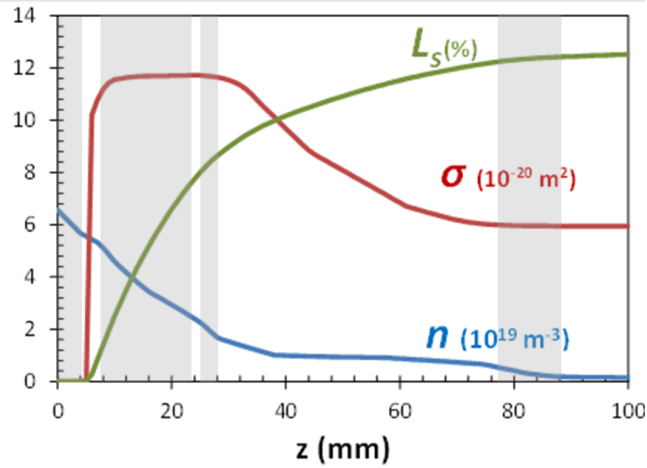


Figure 5 Example of calculated density profile through the RNIS accelerator at room temperature and corresponding cross section  $\sigma$  and stripping losses  $L_s$  in the nominal case of  $V_{ext}=4$  kV,  $V_{acc}=55$  kV. The grid positions are also highlighted by gray box: PG, EG, SG and GG from right to left respectively.

## 5. COMPARISON OF CODES AND EXPERIMENTAL DATA

### 5.1. Estimation of the Beam Current

The electrode voltage and the total extracted beam current are necessary inputs for beam simulations with ray tracing codes. While the voltages are precisely measured at the power supplies, the estimation of the extracted beam current requires some assumptions on electrical or calorimetric measurements. In particular the ion beam current can be extrapolated both from the accelerated current  $I_{ACC}$  (measured as the drain current at the acceleration power supply) and from the thermal power deposited on the MS calorimetric target. In addition, the beam target can be insulated from the grounded vessel, and the current collected on its surface can be measured with a dedicated circuit. Each of these methods has advantages and drawbacks, so that a synergic approach is useful to correctly evaluate the beam current. In the case of RNIS, the acceleration power supply is designed for a current of several ampere, but, during our experiments with a reduced number of beamlets,  $I_{ACC}$  did not exceed 0.5 A and the measurement had poor relative accuracy and was perturbed by leakage currents and by charges generated by the beam gas ionization in the acceleration and drift stage.

On the other side, the current measured on the MS target ( $I_{MS}$ ) is probably a better approximation of the real ion beam current; in fact, the target is located sufficiently far from the accelerator and is not influenced by stray electrons, since the long-range magnetic field (due to filter magnets located in the source) deflects them out, preventing their collection by the target. The beam-induced secondary emission of electrons at the carbon tiles makes necessary a polarization of the calorimeter, to capture emitted particles. The beam impinging the target is composed by  $H^-$ ,  $H^0$  and  $H^+$ , whose fractions depend on the pressure along the accelerator and in the vessel. The determination of the optimal value of the bias voltage of the target tiles is necessary in order to obtain reliable  $I_{MS}$  measurements, as reported in Figure 6a.

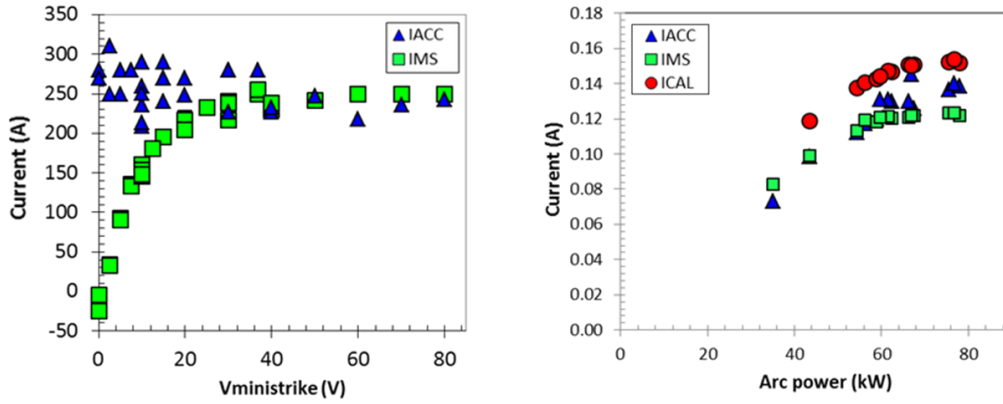


Figure 6: a) current collected by the MiniSTRIKE calorimetric target  $I_{MS}$  as a function of the Bias Voltage applied, b) behaviour of measured current  $I_{ACC}$ ,  $I_{MS}$  and  $I_{CAL}$  with respect to the arc power ( $V_{EXT}=4$  kV,  $V_{ACC}=47.7$  kV).

The characteristic curve in Figure 6a can be explained by distinguishing different contributions to  $I_{MS}$ : i) secondary electrons extracted from the CFC tile by impacting particles, ii) electrons stripped from the  $H^-$  ions during their impact on the tiles, and iii) electrons created by ionization of background gas (henceforth called plasma-electrons). Obviously our aim is to collect the contribution to the current related to the beam (ii), getting rid of the contribution due to secondary electrons and giving an estimate of the plasma-electron contribution.

The plasma-electron current  $I_{PE}$  is created along the path ( $L \approx 0.77$  m) between the GG and the calorimeter, and depends on the gas density  $n_{gas}$  according to the relation  $I_{PE}/I_{H^-} = n_{gas} \sigma L$ ,  $\sigma$  being the ionization cross section for beam impact. In our range of energy and pressure (30-70 keV and 0.01-0.001 Pa respectively) this contribution is always small:  $I_{PE}/I_{H^-} < 5\%$ . On the other side the secondary emission yield of electrons [47] (i) from carbon at 70 keV is high (around 2.5, when  $H^+$  projectile is considered); we can conclude that the purpose of the application of bias voltage to the target tiles is to collect electrons emitted from the graphite and the negative charges stripped from the  $H^-$  during the impact on the tiles. In this sense, the slope of the  $I_{MS}$  in Figure 6a suggests that the spectrum in the re-emitted electrons from  $H^-$  has a peak at low energies: 30V are sufficient to collect the secondary electrons. When the target tile biasing is high enough,  $I_{MS}$  is saturated, and its value is a good estimation of the beam current. We should note that  $I_{MS}$  value is also affected by the presence of positive ions inside the beam (whose contribution is again expected to be low:  $I_{H^+}/I_{H^-} < 1\%$ ) and misses the fraction of ions already converted to neutrals by stripping, so it should be intended as a lower limit of the  $H^-$  current.

Another estimate of the beam current is the calorimetric current  $I_{CAL}$ , which can be obtained from the total energy deposited on the MS target tiles, evaluated by processing the temperatures of the CFC tile recorded by the IR camera. The power deposited by the beam is proportional to the temperature increase of the tile during the interval ranging from the beam-on time ( $t=t_0$ ) to the time at which the maximum temperature on the tile is recorded by the camera ( $t=t_{max}$ ).

The  $I_{CAL}$  measurement relies on the assumption that in these two instants the CFC is completely thermalized in the axial direction, so we can assume that the temperature profile measured on the rear side of the tile is the same as the temperature profile on its front side. In the case of CFC also the non-linear dependence of the specific heat on temperature must be considered. The most accurate method makes use of the total energy difference of the tile during the pulse, defined as

$$\Delta E = E(t_{max}) - E(t_0), \quad (2)$$

where  $E(t)$  is the energy accumulated in the tile at a time  $t$ , expressed as:

$$E(t) = \int \rho \cdot w \cdot C(T(t, x, y)) \cdot T(t, x, y) dx dy \quad (3)$$

$\rho$  being the CFC tile density,  $w$  its thickness,  $T(t, x, y)$  and  $C(T(t, x, y))$  its temperature and specific heat at a given point  $(x, y)$  and at given time  $t$  respectively. The calorimetric current is then evaluated by dividing the energy accumulated in the tile by the pulse length  $\Delta t$  and the total acceleration voltage  $\Delta V$ :

$$I_{CAL} = \frac{\Delta E}{\Delta t \cdot \Delta V} \quad (4)$$

A comparison of  $I_{ACC}$ ,  $I_{MS}$  and  $I_{CAL}$  is reported in Figure 6b, during a scan on the source arc power at constant electrode voltages. The trends of the 3 signals are quite similar, showing the typical saturation of the current plasma density, but the absolute values are different by about 20%. In general, the calorimetrically estimated current  $I_{CAL}$  is expected to give the best approximation of the beam current, the electrical measurements  $I_{ACC}$  and  $I_{MS}$  being affected by stray or secondary particles. This conclusion is also supported by the results of the following section.

## 5.2. Beamlet optics and ion current dependence

The beam current is one of the most critical parameters of ray tracing codes such as OPERA. The shape of the meniscus and the corresponding electrostatic potential distribution are particularly sensitive to variation of the extracted current, especially in the first millimetres after the PG, where the beam density is high. This in turn can produce a large variation of divergence and final radius of the beamlets. In this section we compare the effect of a variation of the beam current on the beam optics in codes and in experiments, keeping constant the values of extraction and acceleration voltage ( $V_{EXT}=4$  kV,  $V_{ACC}=47.7$  kV).

By changing the filament-arc current in the plasma source, we can control the power delivered to the plasma in the source with a direct consequence on the plasma density and consequently on the extracted beam current, as shown in Figure 6b. For each experimental shot having a given arc power, from the IR camera images we estimate the radius  $R$  of the beamlets impinging on the upstream face of the tile, using the inversion and fitting procedures described in section 3.1. The OPERA code is then set up using the experimentally applied voltages, the beam current deduced from the experimental measurements (see section 5.1) and the beam losses due to interaction with the background gas density profile estimated by the AVOCADO code. Using the gas profile together with the appropriate collision cross section [46], in fact, we can model the attenuation of the beam due to electron detachment as shown in Figure 5. Due to the high computational load, only the accelerator region was initially simulated using the OPERA code. In the beam drifting region, the particle trajectories were assumed to follow straight lines (with the exception of the downwards deflection induced by the long range magnetic field, which in any case is not expected to affect beam divergence and size). This approximation was based on the assumption that the beamlet space charge is completely neutralized in the drift region between the accelerator and the calorimeter. However, the results of recent simulations [48], [49] and experiments [50] showed that some space is required for the space charge compensation to set up. In agreement with these findings, also the first 20 mm of the drift region have been included in the OPERA model, in order to take into account this space charge effect. Then, a zero electric field condition has been assumed starting from 20 mm downstream of the GG. The beamlet radius  $R$  at the target is thus calculated using a simple linear relation ( $R=R_0+\delta_0 \cdot L$ ), based on the distance  $L$  between the GG and the target, beamlet radius  $R_0$  and divergence  $\delta_0$  calculated at the end of the OPERA simulation region. We note that, due to the slotted geometry of the GG and SG apertures, the beamlet cross-section is elliptical and the radius and divergence are not the same in the transverse directions, resulting in an elliptical beamlet cross-section at the target; the radii in the horizontal and vertical direction  $R_x$  and  $R_y$  were hence measured and calculated independently. Their values are reported in Figure 7 as a function of the simulated beam current.

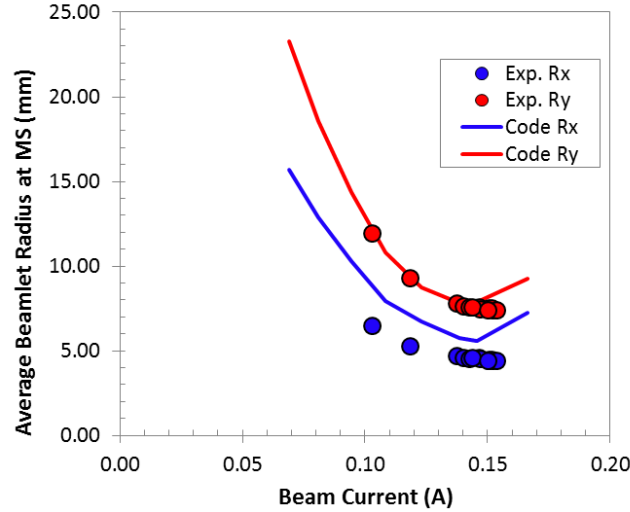


Figure 7 Experimentally measured and numerically modelled size of the beamlets on the miniSTRIKE target, as a function of accelerated beam current ( $V_{EXT}=4$  kV,  $V_{ACC}=47.7$  kV).

The agreement between measured beamlet radius at different  $I_{CAL}$  and the numerical values is satisfactory. The code correctly describes the effect of the asymmetric lens formed at the SG and GG electrodes, causing the vertically elongated shape of the beamlets; the x-divergence (horizontal) results lower than the y-divergence (vertical). For the set of acceleration voltages under consideration, the minimum of both curves is found for a total accelerated beam current of 150 mA, corresponding to a negative ion density of about  $100 \text{ A/m}^2$  at the PG. For lower currents, the penetration of the field in the plasma makes the meniscus too concave, causing the beam divergence to increase. For higher values of current and arc power, the beam space charge in the extractor becomes very high, causing a beam expansion and a partial interception on the SG. These results confirm the hypothesis discussed in section 5.1 that the calorimetric current  $I_{CAL}$  is a good approximation of the accelerated beam current: using another approximation of the beam current would result in a shift of the experimental curve.

### 5.3. Beamlet optics and voltage dependence

The extraction and acceleration voltages are also important parameters governing the beam properties in the accelerator. In fact the ratio  $R_V=V_{ACC}/V_{EXT}$  determines the focusing of the beamlets for a given beam current. In order to keep the beam current constant during the experimental scan, the arc power and extraction voltage were kept constant ( $P_{ARC}=63$  kW,  $V_{EXT}=4$  kV), while the acceleration voltage was varied in the range 40-70 kV. The code was run with the same range of values, and using a fixed beam current of  $100 \text{ A/m}^2$ , resulting from the optimal values found in the arc power scan reported in the previous section. The results of the experimental and of the numerical scans are reported in Figure 8a.

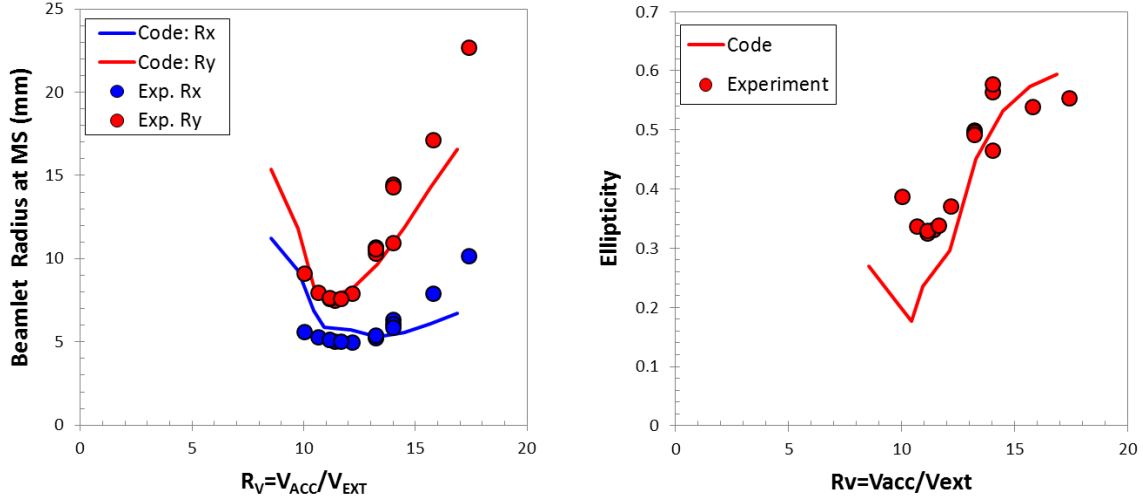


Figure 8 Experimentally measured and numerically modelled beamlet size (left) and ellipticity (right) at the MiniStrike target, as a function of acceleration/extraction voltage ratio. (Beamlet current density=100 A/m<sup>2</sup>; P<sub>ARC</sub>=63 kW,)

Also in this case, the codes were capable of reproducing the beam optics. The trend of the calculated Ry radius (divergence) looks very similar to the measured one, whereas the Rx radius shows a slightly different behaviour, with a more pronounced increase of the beamlet size for increasing  $R_v$ . The value of  $R_v$  ( $\approx 11$ ) corresponding to minimum divergence is anyway in good agreement with the experimental results. We note that the same ratio optimizes both the divergence in the horizontal and vertical directions, motivating the adoption of the racetrack shaped SG in the RNIS in place of a traditional SG with rounded apertures. Unlike the case in which the beam current is varied, when the beam focusing is changed, a clear effect is seen on the shape of the beamlets. In particular, when the acceleration voltage is increased, the y elongated electrostatic lens of the GG is strengthened so that its defocusing action tends to enlarge the beamlet along the vertical direction. This can be clearly seen by plotting the beamlet ellipticity (defined as  $1 - R_x/R_y$ ) against  $R_v$ , as reported in Figure 8b. Also in this case the experimentally measured trend is reproduced by the code, though there is an underestimation of the beamlet distortion at low  $R_v$  values.

#### 5.4. Beamlet Steering and deflection

In the comparison of numerical models against experimental measurements presented in the previous section, the magnetic field has been neglected, since it is expected to have a minor influence on the divergence of the single beamlet; however, this is not true when considering the divergence of the whole beam, unless the non-uniform ion deflection caused by magnetic field is cancelled or mitigated by the displacement of the SG apertures. In this section therefore we quantify the beamlet deflection induced by the magnetic field, and the SG offset that is necessary to compensate for it and recover the straight trajectory of the ion beam.

The magnets embedded in the EG are designed to produce a transverse magnetic field  $B_y$  which deflects the co-extracted electrons toward the upstream surface of the EG. A minor deflection is obviously also suffered by the ions, but in principle one may expect that, thanks to the symmetric  $B_y$  profile guaranteed by the EG magnets layout, the overall ion deflection is almost zero. However, 3 different contributions cause a net deflection of an ion beamlet in the presence of transversal  $B_y$  field: i) the velocity of the ions changes while they pass across the  $B_y$  field, so the effect of the two opposite peaks (see Figure 3) is symmetric only when the integral of the  $B_y$  field along the particle trajectory is zero; ii) upstream of the meniscus, the  $B_y$  effect on ions is shielded by the source plasma, so that, the  $B_y$  field affects the particle trajectories only in the region downstream of the meniscus (where the beam is already formed); therefore the effect of  $B_y$  field is not symmetric, even if the field is symmetric; iii) even assuming that the ion deflection caused by the  $B_y$  field is somehow compensated for, the ion trajectories will be horizontally displaced and will cross the electrostatic lens formed by the EG surface with a certain offset  $dx$ , receiving a deflection  $\phi$  in the opposite direction, according to the thin lens approximation:

$$\varphi = \frac{(E_1 - E_2)}{4V} dx, \quad (4)$$

where  $E_1$  and  $E_2$  are the E field before and after the EG respectively and  $V$  is the EG voltage [51], [52]. The first factor i) causes a beam deflection in the same direction as the electrons, the other two determine a deflection in the opposite direction; the net effect is an ion bending in the opposite direction with respect to the electrons. A detailed theory of the magnetically induced beamlet deflection can be found in [39].

At RNIS, the magnetic deflection of the ion beam is counteracted by a suitable horizontal offset of the SG apertures with respect to the beamlet axis; this offset produces a displacement of the electrostatic lens formed at the SG aperture exit, which, according to eq. (4), corrects the bent beamlet trajectories (steering by aperture displacement). This steering method is the standard procedure adopted to compensate for beamlet deflections also in all existing negative ion based NBIs.

Even if in ITER sources the recovery of the straight ion beam trajectory is achieved by other means [38], the same method is used for instance in the GG of the SPIDER accelerator to counteract the space charge repulsion among beamlets [37]. In SPIDER the offset was estimated using the calculation by the OPERA code, hence it is particularly important to benchmark the code on this point.

With this aim, we included the map of the B field calculated by NBIMAG (whose results were already successfully benchmarked with experiments in section 4.1) into the OPERA model of a single beamlet with  $j=170$  A/m<sup>2</sup>,  $V_{EXT}=4.9$  kV and  $V_{ACC}=61.8$  kV. The effect of the B field and SG steering on the beam motion is quantified as the deflection of the beamlet at the exit of the GG, where both the effects of B field and electrostatic lenses become null; from thereafter the beamlet deflection on the horizontal plane is assumed to be constant (this is not true in the vertical direction, since the long range magnetic filter field generated by the two magnets in the source extends several cm after the GG exit). At first the two opposite effects are evaluated separately. When the SG aperture offset is zero, the beamlet, under the sole influence of the B field, leaves the accelerator with an average deflection of about 9 mrad. On the other hand, when no B field is applied, the beamlet is steered towards the opposite direction with strength proportional to the SG aperture offset. Figure 9 reports the total horizontal deflection of the beamlet at the GG exit for some values of SG offset. These values are fitted with a linear curve, whose slope gives the equivalent steering constant of the SG electrostatic lens: 11.6 mrad/mm.

Using this result, and considering the value of the deflection induced by the  $B_y$  field alone (9 mrad), an offset of the SG apertures of about 0.8 mm in the opposite direction is required to compensate for it. (since  $B_y$  produced by the EG magnets is alternate row by row, the aperture offsets shall also be alternate row by row).

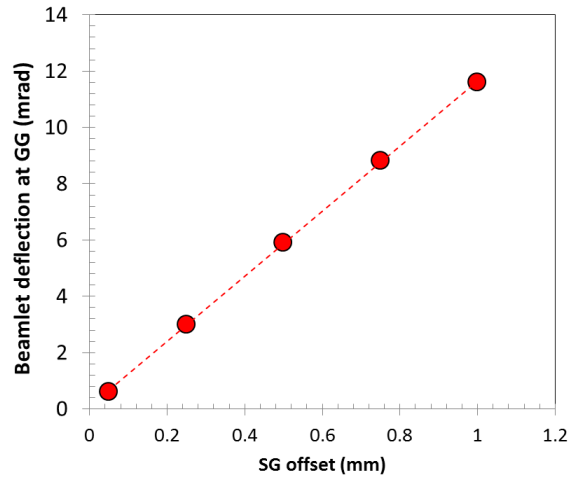


Figure 9 Average beam deflection at the GG exit as a function of the SG aperture offset. B field is not considered in the simulation. Circles indicate numerical simulations with OPERA ( $j=170$  A/m<sup>2</sup>,  $V_{EXT}=4.9$  kV and  $V_{ACC}=61.8$  kV)



The displacement adopted at RNIS was calculated theoretically, and for rounded apertures, before the adoption of the racetrack shape in the SG apertures (having a weaker steering effect). In that case an offset of about 0.5 mm was considered sufficient to compensate for the magnetic deflection. According to OPERA calculation, this value is insufficient, and in fact the experimental results (Figure 10), show a residual beamlet deflection in qualitative agreement with this finding. However, although in better agreement with the experimental results than the analytical estimation on which the SG offset was designed, the OPERA calculation is still underestimating the beam deflection. The measured beamlet deflection  $\vartheta$  at the MS target can be calculated from the results of the IR data fitting, as

$$\vartheta = \tan^{-1}\left(\frac{\Delta x}{2L}\right) \quad (5)$$

Here  $L$  is the distance between the GG and the target, and  $\Delta x$  is the difference between the average horizontal positions of 2 consecutive rows of beamlets. Since there is no reason for a variation of the horizontal beamlet deflection in the drift region, we expect that the measured value of  $\vartheta$  only depends on the beamlet deflection at the accelerator exit. Thus we can compare beamlet deflection  $\vartheta$  measured on the target against OPERA. In principle, the value of  $\vartheta$  depends on total beam energy (as  $E^{-1/2}$  [35]), on the extraction voltage (influencing effects i, and ii), and on the beam space charge; nonetheless, for a given configuration (geometry and B field) these terms usually represent small variation around an average value. Figure 10 shows the measured beam deflection angle as a function of the beam voltage and the deflection angle calculated by OPERA (using the same current and the proper SG offset, solid red line). From the difference between numerical results and experimental data one may conclude that the code is missing part of the physics, so that the magnetic deflection of the beamlet is underestimated by almost a factor of 2. A possible explication for this discrepancy is discussed in the last section of the paper.

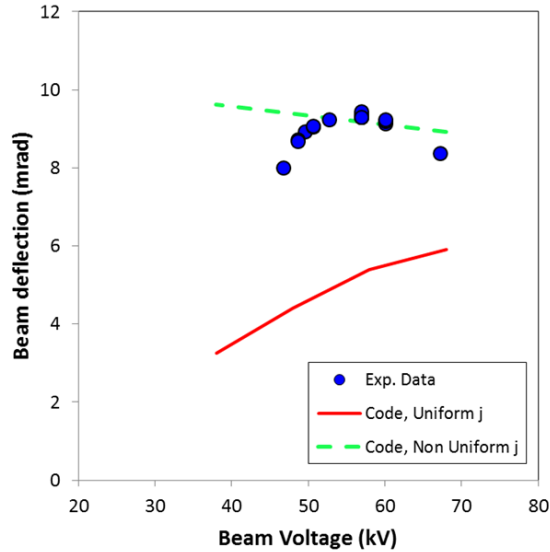


Figure 10. Measured and calculated average beam deflection (with uniform and non-uniform extracted current distribution).

## 5.5. Beam Transport and multi-beamlet interaction

All the intermediate data generated by the codes described so far are also needed to have a detailed view on the beam transport of the beam along the beamline and of the power deposition phenomena involved in this process. The particle trajectories and the heat loads along the accelerator and the drift region are calculated on the basis of the electric potential map, magnetic fields and gas density distribution. The EAMCC-3D code models the propagation



of negative ions from the extraction region (meniscus) to the CFC target surface. The code is capable of calculating the generation rate of secondary particles, and to track their trajectories in the electromagnetic fields, up to the computation of the power deposition on material surfaces. For a direct benchmark of the code results with the experiment, an evaluation of the calorimetric data (temperature rise of the cooling water on each electrode) is needed. In the RNIS campaign, anyway, this was not possible since the reduced number of electrode apertures in operation translates in very low heat loads ( $\sim 10$  kW), if compared to the capabilities of the cooling plant ( $\sim$  MW), so that the estimation of the averaged power per electrode is not precise. Even if the estimation of heat loads is the main purpose to use this code and a specific comparison on this point is highly advisable (a test on the basic version is reported in [53]), EAMCC-3D is used because it can also model the propagation of the beam in the beamline volume, overcoming some intrinsic restrictions of the OPERA code, where the solution of Poisson equation poses a limit on the reasonable number of particles and domain size. At first the space charge problem in the presence of B field, is solved by OPERA for 15 beamlet, with a reduced number of macro-particles ( $< 10^4$ ), and limited to the accelerator domain. Then the electric potential map is exported to EAMCC-3D, and enlarged to include the space charge compensation region (drift region of the beam line), by smoothly imposing a vanishing E field few centimetres after the exit of the GG. Then EAMCC-3D is run with large number of particles ( $> 1e7$ ). This approach has the advantage of completely accounting for electrostatic effects in the accelerator (deflections, divergence, beamlet-beamlet interactions) and the long range stray magnetic field throughout the beamline.

Same sample trajectories of negative ions and secondary particles calculated by EAMCC-3D are reported in Figure 11. The vertical deflection under the effect of the long range B field of beam and secondary particles is clearly visible. Stray electrons created in the accelerator and deflected out of the beam in the first 200 mm of the drift tube are also visible. At about  $z=200$  mm, the Bx component reverses its direction, so that electrons stripped after that point are deflected upward. Just very few electrons reach the MS calorimeter target, justifying their absence from the contributions to  $I_{MS}$  in section 5.1.

From the macro-particle distribution at the exit plane, we can deduce the simulated beamlet pattern on the upstream surface of the MS calorimeter tiles. These data have been compared with the measured profile (reconstructed from the IR data, as discussed in section 3.1). The corresponding power density map is reported in Figure 12.

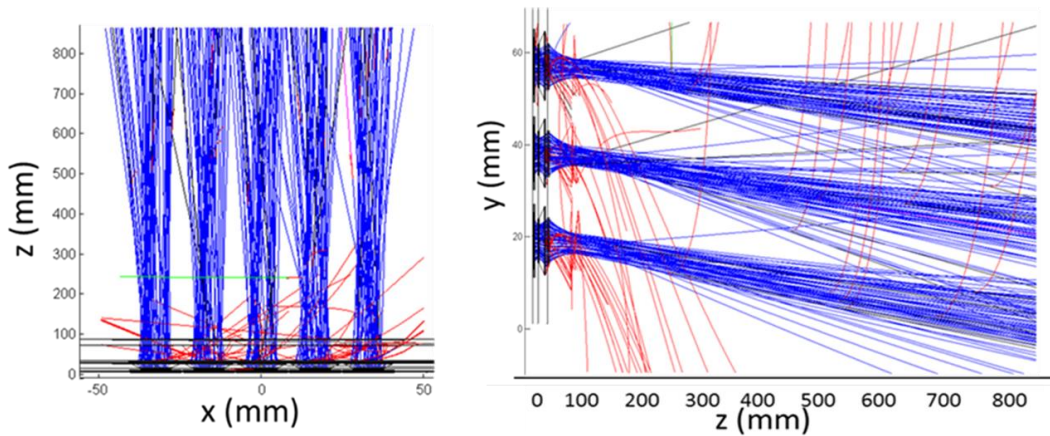


Figure 11 *Beamlet trajectories (H<sup>-</sup> in blue, electrons in red) calculated with EAMCC-3D inside the accelerator (from  $z=0$  to  $z=90$  mm) and in the drift region between the GG and MS ( $z=860$  mm).*

A clear correlation exists among the measured and calculated beam power density patterns on the MS target, as evident from the comparison of Figure 2 and Figure 12. The average vertical deflection is in agreement with the measured one. The zig-zag pattern, i.e. the beamlet offset due to the non-perfect compensation of the magnetic deflection by SG aperture displacement is correctly reproduced. However, the experimentally measured beamlet offset is around a factor of 2 larger than the simulation result, reflecting the findings of the previous section concerning the beamlet deflection, underestimated by a factor of two.

Another issue to be investigated is the alignment of the different rows of beamlets, which in the measured profile seems to be slightly rotated along opposite directions on a row basis; this effect is not present in the simulated profile. This aspect needs further investigation, but again, since the rotation is clearly correlated with the magnets

embedded in the EG (the rotation is alternated row by row), whose value is correctly reproduced by the magnetic codes, we may in principle argue that the reason may lie in the distribution of the currents at the meniscus.

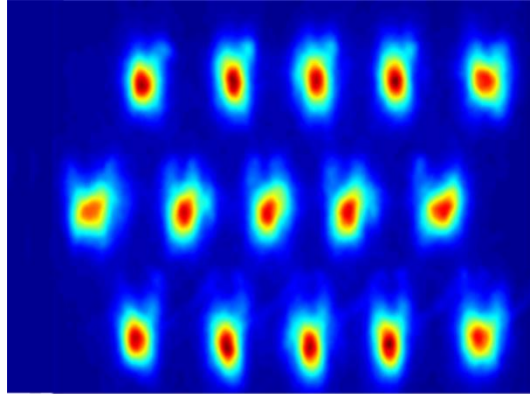


Figure 12 Simulated power density profile on the upstream side of MS target obtained with EAMCC-3D.

### 5.6. Beamlet current density uniformity

The uniformity of the extracted H<sup>-</sup> current density deserves a separate discussion. A possible reason of the discrepancy found in sections 5.4 and 5.5, in fact, is the uniform H<sup>-</sup> extracted current distribution, which is assumed in the OPERA and EAMCC codes. In a previous work [54] it was shown that a non-uniform distribution of H<sup>-</sup> at PG aperture (i.e. H<sup>-</sup> more concentrated on the ExB side of the aperture) results in a net deflection of the beamlet in the opposite direction. This non uniformity is justified by Gutser [55] as the effect of gyration radius on H<sup>-</sup> particles located on opposite sides of the PG aperture, caused by the influence of the magnetic field on the particle upstream of the PG. Additional OPERA simulations using a non-uniform emitter of H<sup>-</sup> particles as proposed by Gutser (45% current inhomogeneity in place of the standard uniform emitter), showed that beamlet deflection can effectively be enhanced by this effect. The results are reported in Figure 10 (green slashed line) together with the results obtained when uniform current is used in OPERA; the meniscus is reported in Figure 13; its shape reflects the asymmetry in the current distribution and is responsible for an additional beam deflection at PG exit. The overall calculated deflection shows a better agreement with the measured values of  $\vartheta$ , as reported in Figure 10a (green line). We also note that the assumption of non-uniform meniscus affects the beam divergence only to a minor extent, so that the beam optics that was found in agreement with the experiments in the previous sections is compatible with this hypothesis.

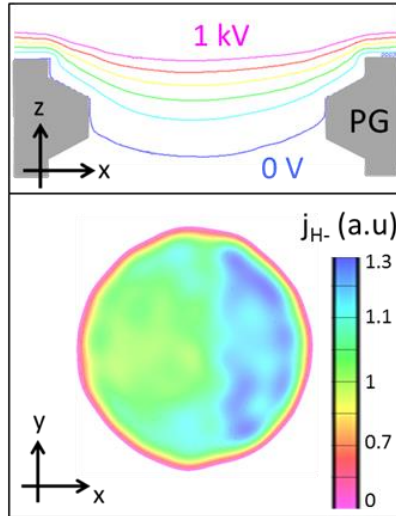


Figure 13 In a) the meniscus shape ( $V=0$  equipotential line) in the  $xz$  plane is shown. In b) the distribution of the current at the meniscus is reported.

## 6. CONCLUSIONS

A benchmark of the set of numerical codes used for modelling negative beam acceleration, transport, and interaction with the mechanical structures was presented. For the first time, a coherent analysis of powerful beam propagation, from its extraction from the plasma, to the impact of the accelerated particle on the calorimeter was presented. The set of codes discussed is the same used in the design of the ITER HNB, and was applied to the case of the RNIS facility at NIFS institute and compared with experimental results. The models used for the simulation of the magnetic field distribution exhibit a high reliability, as resulting from the direct comparison of their results with measured values. The application of a molecular flow code (AVOCADO) to a real vacuum system of nuclear fusion application was carried out: the measured gas pressures in the ion source and in the vessel, and the metering valve settings controlling the injected throughput were used as benchmarks for the simulation showing a small discrepancy, and highlighting uncertainties due to the operation in transient conditions of the ion source. The gas density profile along the accelerator was then included in the beamline models to calculate the  $H^-$  beam losses. The beam optics calculated with the ray tracing code OPERA shows a reasonable agreement with the experimental data, both in terms of beam space charge (current density) and focusing dependences. A careful estimation of the extracted beam current was fundamental to allow the comparison, and the availability of different diagnostics was important in this sense. The beam loss due to stripping caused by the gas density along the accelerator was included in the simulation to allow a more precise calculation of the beam space charge. A less satisfactory agreement was found concerning the simulation of beamlet deflection induced by magnetic and electrostatic effects, which appears to be underestimated by a factor of  $\sim 2$  with respect to the experimental results. Since magnetic fields are measured exactly, the motivation of such discrepancy most likely resides in aspects not yet included in the OPERA code. A possible explanation, based on non-uniform  $H^-$  extraction caused by the magnetic field, was proposed. This specific topic is of particular interest and surely deserves further investigations. The impact on such underestimation in the beam deflection may have an impact on ITER HNB, where the maximum tolerable horizontal misalignment is only 2 mrad, even if, thanks to the much higher voltage used in that case (up to 1 MV) any deflection tends to be reduced.

From the point of view of the beam transport through the accelerator and up to the calorimeter, simulated with the modified EAMCC code, a reasonable affinity with the IR data was found. Nonetheless some open points still needs further investigations, such as the alignment of the beamlet belonging to the same row, whose cause is not reproducible with the set of codes used so far. More in general, the use of the CFC calorimeter for the aim of the code benchmark was satisfactory, and the diagnostics showed a high reliability if a proper post processing of IR

images is provided. These results further motivate the construction of the full scale diagnostic calorimeter STRIKE, under development for the SPIDER experiment.

## 7. ACKNOWLEDGMENTS

Contribution by Consiglio Nazionale delle Ricerche and Japan Society for the Promotion of Science is acknowledged. The collaboration and the partial financial support of F4E is also acknowledged. This work has been carried out within the framework of the EUROfusion Consortium and has received funding from the Euratom research and training programme 2014-2018 under grant agreement No 633053. The views and opinions expressed herein do not necessarily reflect those of the European Commission.

## 8. BIBLIOGRAPHY

- [1] R. Zorat and D. Venders, "Global model for an rf hydrogen inductive plasma discharge in the deuterium negative ion source experiment including negative ions," *Journal of Physics D: Applied Physics*, vol. 33, no. 14, 2000.
- [2] M. Cavenago and S. Petrenko, "Models of radiofrequency coupling for negative ion sources," *Rev Sci Instrum.*, vol. 83, no. 2, 2012.
- [3] M. Cazzador, M. Cavenago, G. Serianni and P. Veltri, "Semi-analytical modeling of the NIO1 source.," *AIP Conference Proceedings of the Fourth International Symposium on Negative Ions Beam and Sources (NIBS2014)*, vol. 1655, no. 1, p. 020014, 2015.
- [4] G. J. M. Hagelaar, G. Fubiani and J. Boeuf, "Model of an inductively coupled negative ion source: I. General model description," *Plasma Source Science and Technology*, vol. 20, no. 1, 2011.
- [5] A. Shivarova, D. Todorov and S. Lishev, "Self-induced steady-state magnetic field in the negative ion sources with localized rf power deposition.," *Rev. Sci. Instrum.*, vol. 87, no. 2, p. 02B308, 2016.
- [6] R. Gutser, Experiments and Simulations for the Dynamics of Cesium in Negative Hydrogen Ion Sources for ITER N-NBI, Doctoral dissertation, Augsburg University, 2010.
- [7] S. Mochalsky, D. Wunderlich, B. Ruf, P. Franzen, U. Fantz and T. Minea, "3D numerical simulations of negative hydrogen ion extraction using realistic plasma parameters, geometry of the extraction aperture and full 3D magnetic field map," *Rev. Sci. Instrum.*, vol. 85, p. 02B301, 2014.
- [8] F. Taccogna, P. Minelli and S. Longo, "Three-dimensional structure of the extraction region of a hybrid negative ion source," *Plasma Sources Science and Technology*, vol. 22, no. 4, p. 045019, 2015.
- [9] I. Goto, K. Miyamoto, S. Nishioka and A. Hatayama, "Study of the negative ion extraction mechanism from a double-ion plasma in negative ion sources," *AIP Conf. Proc. of fourth International Symposium on Negative Ions, Beam and Sources*, vol. 1655, p. 020011, 2015.
- [10] J. P. Boeuf, G. Fubiani and L. Garrigues, "Issues in the understanding of negative," *Plasma Source Science and Technology*, vol. 25, p. 045010, 2016.
- [11] J. Pamela, "A model for negative ion extraction and comparison of negative ion optics

- calculations to experimental results,” *Review of Scientific Instruments*, vol. 62, no. 5, p. 1163, 1991.
- [12] OPERA-3D, Cobham plc, Brook Road, Wimborne, Dorset, BH21 2BJ, UK, [Online]. Available: <http://operafea.com/>.
- [13] P. Agostinetti, G. Chitarin, P. Franzen, B. Ruf, G. Serianni and P. Veltri, “Benchmark of the SLACCAD code against data from the MANITU testbed at IPP,” *AIP Conf. Proc. of the Third Symposium on Negative Ions, Beam and Sources*, vol. 1515, p. 522, 2013.
- [14] P. Agostinetti, M. Giacomini, G. Serianni, P. Veltri, F. Bonomo and L. Schiesko, “Preliminary results concerning the simulation of beam profiles from extracted ion current distributions for mini-STRIKE,” *Rev. Sci. Instrum.*, vol. 87, p. 02B913, 2016.
- [15] P. Veltri, V. Antoni, P. Agostinetti, M. Brombin, K. Ikeda, M. Kisaki, H. Nakano, E. Sartori, G. Serianni, Y. Takeiri and K. Tsumori, “Optics of the NIFS negative ion source test stand by infrared calorimetry and numerical modelling,” *Rev. Sci. Instrum.*, vol. 87, p. 02B908, 2016.
- [16] R. Hemsworth and e. al., “Status of the ITER heating neutral beam system,” *Nuclear Fusion*, vol. 49, p. 04500, 2009.
- [17] H. d. Esch, M. Kashiwagi, M. Taniguchi, T. Inoue., G. Serianni, P. Agostinetti, G. Chitarin, N. Marconato, E. Sartori, P. Sonato, P. Veltri, N. Pilan, D. Aprile, N. Fomesu, V. Antoni, M. Singh, R. S. Hemsworth and M. Cavenago, “Physics design of the HNB accelerator,” *Nuclear Fusion*, vol. 55, p. 096001, 2015.
- [18] V. Toigo and e. al., “Progress in the realization of the PRIMA neutral beam test facility,” *Nuclear Fusion*, vol. 55, no. 8, p. 083025, 2015.
- [19] P. Agostinetti, D. Aprile, V. Antoni, M. Cavenago, G. Chitarin, H. d. Esch, A. D. Lorenzi, N. Fomesu, G. Gambetta, R. Hemsworth, M. Kashiwagi, N. Marconato, D. Marcuzzi, N. Pilan, E. Sartori, G. Serianni, M. Singh, P. Sonato, E. Spada and V. Toigo, “Detailed design optimization of the MITICA negative ion accelerator in view of the ITER NBI,” *Nuclear Fusion*, vol. 56, no. 1, 2015.
- [20] M. Cavenago, P. Veltri, F. Sattin, G. Serianni and a. V. Antoni, “Negative Ion Extraction With Finite Element Solvers and Ray Maps,” *IEEE Transaction on Plasma Science*, vol. 36, no. 4, 2008.
- [21] P. Veltri, M. Cavenago and G. Serianni, “A 2D Particle in Cell model for ion extraction and focusing in electrostatic accelerators,” *Rev. Sci. Instrum.*, vol. 82, no. 2, p. 02A711, 2014.
- [22] G. Chitarin, M. Guarnieri and A. Stella, “An integral formulation for eddy current analyses in axisymmetric configurations,” *IEEE Trans. Magnetics*, vol. 25, p. 4330, 1989.
- [23] E. Sartori and P. Veltri, “AVOCADO: A numerical code to calculate gas pressure distribution,” *Vacuum*, vol. 90, pp. 80-88, 2013.
- [24] G. Saksaganski, *Molecular flow in complex vacuum systems*, New York: Gordon and Breach, 1988.
- [25] E. Sartori, S. D. Bello, M. Fincato, W. Gonzalez, G. Serianni and P. Sonato, “Browse Journals & Magazines > IEEE Transactions on Plasma S ...> Volume:42 Issue:9 Help Working with Abstracts,” *IEEE Transactions on Plasma Science*, vol. 42, no. 9, 2014.
- [26] E. Sartori, P. Veltri, M. Cavenago and G. Serianni, “Background gas density and beam

- losses in NIO1 beam source,” *Rev. Sci. Instrum.*, vol. 87, p. 02B118, 2016.
- [27] E. Sartori, P. Agostinetti, S. D. Bello, D. Marcuzzi, G. Serianni, P. Sonato and P. Veltri, “Comparative study of beam losses and heat loads reduction methods in MITICA beam source,” *Rev. Sci. Instrum.*, vol. 85, p. 02B308, 2014.
- [28] G. Fubiani, H. d. Esch, A. Simonin and a. R. Hemsworth, “Modeling of secondary emission processes in the negative ion based electrostatic accelerator of the International Thermonuclear Experimental Reactor,” *Phys. Rev. ST Accel. Beams*, vol. 11, p. 014202, 2008.
- [29] P. Veltri, P. Agostinetti, M. D. Palma, E. Sartori and G. Serianni, “Evaluation of power loads on MITICA beamline components due to direct beam interception and electron backscattering,” *Fusion Engineering and Design*, vol. 88, no. 6, pp. 1011-1014, 2013.
- [30] E. Sartori, P. Veltri, G. Serianni, M. D. Palma and G. C. a. P. Sonato, “Modeling of Beam Transport, Secondary Emission and Interactions With Beam-Line Components in the ITER Neutral Beam Injector,” *IEEE Transactions on Plasma Science*, vol. 42, no. 3, pp. 633-639, 2014.
- [31] V. Antoni, P. Agostinetti, D. Aprile, M. Cavenago, G. Chitarin, N. Fonnesu, N. Marconato, N. Pilan, E. Sartori, G. Serianni and P. Veltri, “Physics design of the injector source for ITER neutral beam injector,” *Rev Sci Instrum.*, vol. 85, no. 2, p. 02B128, 2014.
- [32] N. Fonnesu, P. Agostinetti, G. Serianni, M. Kasaki and P. Veltri, “A multi-beamlet analysis of the MITICA accelerator,” *AIP Conf. Proc. of fourth International symposium on Negative Ions, Beams and Sources*, vol. 1655, p. 050008, 2014.
- [33] N. Fonnesu, M. Cavenago, G. Serianni and P. Veltri, “Particle transport and heat loads in NIO1,” *Rev. Sci. Instrum.*, vol. 87, p. 02B905, 2016.
- [34] J. Conrad, “Beamlet steering by aperture displacement in ion sources with large acceleration deceleration ratio,” *Rev. Sci. Instrum.*, vol. 51, p. 418, 1980.
- [35] R. Hamabe and al., “Compensation of beam deflection due to the magnetic field using beam steering by aperture displacement technique in the multibeamlet negative ion source,” *Rev. Sci. Instrum.*, vol. 72, no. 8, 2001.
- [36] Y. Takeiri, O. Kaneko, Y. Oka, K. Tsumori, E. Asano, R. Akiyama, T. Kawamoto, T. Kuroda and A. Ando.
- [37] P. Agostinetti, V. Antoni, M. Cavenago, G. Chitarin, N. Marconato, D. Marcuzzi, N. Pilan, G. Serianni, P. Sonato, P. Veltri and a. P. Zaccaria, “Physics and engineering design of the accelerator and electron dump for SPIDER,” *Nuclear Fusion*, vol. 51, p. 063004, 2011.
- [38] C. G., A. P., A. D., M. N. and V. P., “Cancellation of the ion deflection due to electron-suppression magnetic field in a negative-ion accelerator,” *Rev. Sci. Instrum.*, vol. 85, p. 02B317, 2014.
- [39] M. Cavenago and P. Veltri, “Deflection compensation for multiaperture negative ion beam extraction: analytical and numerical investigations,” *Plasma Sources Sci. Technol.*, vol. 23, p. 065024, 2014.
- [40] K. Tsumori, M. Osakabe, O. Kaneko, Y. Takeiri, K. Nagaoka, Y. Oka, K. Ikeda, M. Shibuya, E. Asano, S. Komada, T. Kondo and M. Sato, “Neutral beam injection with an improved accelerator for LHD,” *Rev Sci Instrum.*, vol. 79, no. 2, p. 02C107, 2008.

- [41] K. Tsumori, O. Kaneko, Y. Takeiri, Y. Oka, M. Osakabe, K. Ikeda, K. Nagaoka, T. Kawamoto, E. Asano, M. Sato, T. Kondo, J. Watanabe, S. Asano and Y. Suzuki, "Correction of Beam Distortion in Negative Hydrogen Ion Source with Multi-Slot Grounded Grid," *AIP Conf. Proc.*, vol. 763, no. 35, 2005.
- [42] A. Rizzolo, M. D. Palma, M. D. Muri and G. Serianni, "Design and analyses of a one-dimensional CFC calorimeter for SPIDER beam characterisation," *Fusion Engineering and Design*, vol. 85, no. 10–12, p. 2268–2273, 2010.
- [43] G. Serianni, F. Bonomo, M. Brombin, V. Cervaro, G. Chitarin, S. Cristofaro, R. Delogu, M. D. Muri, D. Fasolo, N. Fomesu, L. Franchin, P. Franzen, R. Ghiraldelli, F. Molon, A. Muraro, R. Pasqualotto, B. Ruf, L. Schiesko, M. Tollin and P. Veltri, "Negative ion beam characterisation in BATMAN by mini-STRIKE: Improved design and new measurements," *AIP Conf. Proc.*, vol. 1655, p. 060007, 2015.
- [44] R. S. Delogu, C. Poggi, A. Pimazzoni, G. Rossi and G. Serianni, "Analysis of diagnostic calorimeter data by the transfer function technique," *Rev. Sci. Instrum.*, vol. 87, p. 02B932, 2016.
- [45] Chitarin, P. Agostinetti, A. Gallo, N. Marconato, H. Nakano, G. Serianni, Y. Takeiri and K. Tsumori, "Experimental mapping and benchmarking of magnetic field codes on the LHD Ion Accelerator," *AIP Conference Proceedings*, vol. 1390, pp. 381-390, 2011.
- [46] C.F. Barnett, Atomic Data for Fusion. Volume 1: Collisions of H, H<sub>2</sub>, He, and Li Atoms and Ions with Atoms and Molecules, ORNL-6086, 1990.
- [47] R. Langley, J. Bohdansky, W. Eckstein, P. Mioduszewski, J. Roth, E. Taglauer, E. Thomas, H. Verbeek and K. Wilson, "Data Compendium for Plasma- Surface Interaction," *Nuclear Fusion*, vol. 24, 1984.
- [48] P. Veltri, M. Cavenago and G. Serianni, "Spatial characterization of the space charge compensation of negative ion beams," *AIP Conf. Proc.*, vol. 1515, p. 541, 2013.
- [49] E. Sartori, T. J. Maceina, P. Veltri, M. Cavenago and G. Serianni, "Simulation of space charge compensation in a multibeamlet negative ion beam," *Rev. Sci. Instrum.*, vol. 87, p. 02B917, 2016.
- [50] F. Bonomo, B. Ruf, M. Barbisan, S. Cristofaro, L. Schiesko, U. Fantz, P. Franzen, R. Pasqualotto, R. Riedl, G. Serianni, D. Wunderlich and t. NNBI-Team, "BATMAN beam properties characterization by the beam emission spectroscopy diagnostic," *AIP Conf. Proc.*, vol. 1655, p. 060009, 2015.
- [51] C. Davison and C. Calbick, "Electron lenses," *Phys. Rev.*, vol. 38, p. 585, 1931.
- [52] P. Veltri, P. Agostinetti, D. Marcuzzi, E. Sartori and G. Serianni, "The influence of grid positioning on the beam optics in the neutral beam injectors for ITER," *Fusion Engineering and Design*, vol. 107, pp. 64-69, 2016.
- [53] G. Fubiani, R. S. Hemsworth, H. P. L. d. Esch and L. Svensson, "Analysis of the two accelerator concepts foreseen for the neutral beam injector of the International Thermonuclear Experimental Reactor," *Phys. Rev. ST Accel. Beams*, vol. 12, p. 050102, 2009.
- [54] P. Veltri, P. Agostinetti, G. Serianni, V. Antoni and M. Cavenago, "Effects of Negative Ion Source Characteristics on Beam Optics: The Case of SPIDER," *IEEE Transactions on*

*Plasma Science*, vol. 40, no. 9, pp. 2279-2284, 2012.

[55] R. Gutser, D. Wunderlich and U. Fantz, "Negative hydrogen ion transport in RF-driven ion sources for ITER NBI," *Plasma Physics and Controlled Fusion*, vol. 51, p. 045005, 2009.